Computational Elastography from Standard Ultrasound Image Sequences by Global Trust Region Optimization

Jan Kybic[1] and Daniel Smutek[2]

[1] Center for Machine Perception, Czech Technical University, Prague, Czech Republic
kybic@fel.cvut.cz,
http://cmp.felk.cvut.cz/~kybic
[2] Faculty of Medicine I, Charles University, Prague, Czech Republic

Abstract. A new approach is proposed to estimate the spatial distribution of shear modulus of tissues in-vivo. An image sequence is acquired using a standard medical ultrasound scanner while varying the force applied to the handle. The elastic properties are then recovered simultaneously with the inter-frame displacement fields using a computational procedure based on finite element modeling and trust region constrained optimization. No assumption about boundary conditions is needed. The optimization procedure is global, taking advantage of all available images. The algorithm was tested on phantom, as well as on real clinical images.

1 Introduction

Elastography, or elasticity imaging [1, 2], aims at noninvasive measurement of elastic properties of tissues and their spatial distributions. Knowing elastic parameters can be very useful for biomedical modeling as well as for diagnostics. As an example, many carcinoma are harder than the surrounding healthy tissue [3–5], as are some lesions. It has been established that several diseases of breast, kidney, prostate, blood vessels and other organs are also accompanied by a change of elastic properties of tissues. After all, palpation, a precursor to elastography, has been used for medical diagnosis since perhaps several thousand years.

Many kinds of elastographic procedures have been proposed in recent years [6–10]. In most cases, a small force is applied to the tissue and the resulting displacement is measured. Typically, the induced displacement is extremely small and a special device is needed to measure it. In ultrasound based elastography, we often need to resolve displacements significantly smaller than the wavelength. A special ultrasound scanner is used, allowing the sampling of the received signal (RF signal) at very high frequency [11–13], so that it can be correlated with the emitted pulse.

However, such specialized devices are not yet readily available in clinical practice. Therefore, we attempt to develop an elastography approach using only

a standard ultrasound machine, without any special hardware. The tissue is deformed by varying the force applied by the operator on a standard ultrasound hand-held transducer while acquiring the image sequence. A specialized reconstruction algorithm is used, simultaneously estimating the shear modulus distribution and the displacement fields between a chosen reference frame and the rest of the images in the sequence.

We have already confirmed the feasibility of reconstructing elastic properties of tissues from standard ultrasound images in our previous work [14], where we have used a pair of images for the reconstruction. Like all similar methods described in the literature [8–10, 15], we were forced to provide stress (force) boundary conditions for the elasticity problem even on the virtual internal boundaries of the imaged region, where no measurement is available. Using displacement-only boundary conditions leads to an inherently ill-posed and unstable inverse problem, even if additional boundary conditions for the elastic modulus μ are imposed [16]. In practical terms it means that there are many different modulus distributions consistent with the two acquired images within measurement accuracy.

The new reconstruction algorithm described here can find a shear modulus distribution μ consistent with a whole set of images, allowing us to choose a trade-off between the robustness and accuracy of the estimation and the time and memory requirements. The applied force does no longer have to be strictly perpendicular to the sensor array, maintaining the same image plane is enough. Moreover, no assumptions are needed about the boundary forces any more. By virtue of using more images, the problem is better posed. It has been shown recently [17] that the elastic modulus can be reconstructed almost uniquely (up to 4 constants) from two displacement fields, i.e. 3 images in our case, and up to 1 constant from 4 displacement fields (5 images). To the best of our knowledge, this is the first algorithm described in the literature that combines information from several images (or equivalently, from several displacement fields), to reconstruct elasticity parameters.

2 Method

2.1 Data acquisition

An ultrasound probe (transducer) of a Philips Envisor scanner is placed on a skin above the zone of interest, such as the thyroid gland, breast, or liver. An image sequence of about 10 s at $5 \sim 10$ frames per second is acquired while the operator slowly varies the pressure applied on the handle. The operator is instructed to keep the same image plane as closely as possible. Out of this sequence, a smaller number of approximately equidistant images (in time) are selected for further processing, ideally with no motion and other artifacts. The selected 2D images will be denoted f_t for $-n_1 \leq t \leq n_2$. Image f_0 will be called a reference image. The images of an area denoted Ω are taken in a moving coordinate system attached to the sensor (Figure 1).

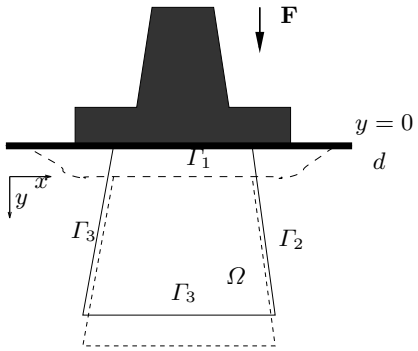

Fig. 1. The tissue is deformed by varying the pressure on the ultrasound probe (black). Dashed lines show the position of the skin and the sensed region after the probe is shifted (in this case downward by a distance d).

2.2 Elasticity equations

Let us consider the tissue movement between two adjacent images f_{t_-}, and f_t, where $t_- = t - \operatorname{sign} t$. In other words, f_{t_-} is the image preceding f_t towards the reference image f_0. Since we do not have any information about the movement of the tissue outside the imaging plane, we will make the standard assumption of a *plane strain*, i.e. that all the out-of-plane strains (displacements) are zero. Let us denote $\mathbf{v}_t$ the displacement field between f_{t_-} and f_t

$$\mathbf{v}_t\big(\mathbf{u}_{t_-}(\mathbf{x})\big) = \mathbf{u}_t(\mathbf{x}) - \mathbf{u}_{t_-}(\mathbf{x}) \tag{1}$$

where $t \mapsto \mathbf{u}_t(\mathbf{x})$ is the trajectory of a tissue point that is at coordinates $\mathbf{x}$ in frame f_0; $\mathbf{u}_0(\mathbf{x}) = \mathbf{x}$. Note that $\mathbf{v}_t$ is expressed in the coordinate system of f_{t_-}. We shall assume that the displacement is small and that the tissue is isotropic and incompressible. Then, the displacement field satisfies the standard elasticity equations [1, 10] governed by a Lamé parameter $\mu(\mathbf{x}) > 0$, the shear modulus:

$$\left.\begin{aligned} -\nabla p_t + \nabla \cdot \big(2\mu \nabla^s \mathbf{v}_t\big) &= \mathbf{0} \\ -\nabla \cdot \mathbf{v}_t &= 0 \end{aligned}\right\} \quad \text{in } \Omega \tag{2}$$

where p_t is a pressure, positive for compression, and $\boldsymbol{\varepsilon}_t = \nabla^s \mathbf{v}_t = \frac{1}{2}(\nabla \mathbf{v}_t + \nabla \mathbf{v}_t^T)$ is a symmetric strain tensor. Note that there are $n = n_1 + n_2$ independent displacements $\mathbf{v}_t$ and pressures p_t, one for each image f_t, $t \neq 0$, while there is only one field μ, defined in the reference coordinate system, common to all images. All equations (2) must be satisfied simultaneously, for all images t, $-n_1 \leq t \leq n_2$, $t \neq 0$. The only boundary condition we impose is

$$\mathbf{u}_t = \mathbf{v}_t = \mathbf{0} \qquad \text{on } \Gamma_1 \tag{3}$$

It comes from the assumption that the ultrasound sensor is always in touch with the upper edge Γ_1 of the imaged region Ω (the skin).

2.3 Weak formulation

We convert the strong formulation (2) into an equivalent weak one [10]. We say that fields $\mu \in L^+_\infty(\Omega)$, $\{\mathbf{v}_t\} \in H_1(\Omega)^n$, $\{p_t\} \in L_2(\Omega)^n$, are consistent with the elasticity constraints, iff (3) holds and

$$\begin{aligned} 0 = A\big(\mu; \{\mathbf{v}_t\}, \{p_t\}, \{\mathbf{w}_t\}, \{q_t\}\big) &\stackrel{\text{def}}{=} \sum_{t\neq 0} A_t(\mu; \mathbf{v}_t, p_t, \mathbf{w}_t, q_t) \\ A_t(\mu; \mathbf{v}_t, p_t, \mathbf{w}_t, q_t) &= \int_\Omega 2\mu_t \nabla^s \mathbf{v}_t : \nabla^s \mathbf{w}_t - (\nabla\cdot\mathbf{w}_t)p_t - (\nabla\cdot\mathbf{v}_t)q_t \,\mathrm{d}\Omega \end{aligned} \tag{4}$$

for all sufficiently regular and integrable test functions $\mathbf{w}_t \in H^1(\Omega)$ and $q_t \in L_2(\Omega)$ such that $\mathbf{w}_t = \mathbf{0}$ on $\partial\Omega$. We write

$$\boldsymbol{\xi} \stackrel{\text{def}}{=} \big(\mu, \{\mathbf{v}_t\}, \{p_t\}\big) \in \mathcal{C} \quad \Longleftrightarrow \quad \forall \mathbf{w}_t, q_t;\ A\big(\mu; \{\mathbf{v}_t\}, \{p_t\}, \{\mathbf{w}_t\}, \{q_t\}\big) = 0 \tag{5}$$

where $\mathcal{C}$ is a manifold representing all consistent modulus, displacement, and pressure fields. Note that no boundary conditions are imposed apart from (3).

2.4 Finite element method

We convert the continuous formulation (4) to a corresponding linear system of equations using the Galerkin method [18]. The domain Ω is triangulated to form a mesh with a maximum edge size h.The mesh topology is the same for all frames, while the mesh nodes follow the tissue, i.e. the trajectory of a node with an initial position $\mathbf{x}$ (corresponding to the reference frame) is $\mathbf{u}_t(\mathbf{x})$. We shall denote N_v the total number of vertices in the mesh, N_u the number of vertices except the top, non-moving edge, and N_i the number of internal vertices, not lying on any edge.

The modulus μ, the displacement fields $\mathbf{v}_t$ and the test functions $\mathbf{w}_t$ are discretized with P1 basis functions φ_i (equal to 1 at vertex i, 0 on other vertices, and piecewise linear on each triangle). The pressure p_t and test functions q_t are discretized with P0 basis functions ψ_i (piecewise constant):

$$\mu^h = \sum_i \mathrm{m}_i \varphi_j \qquad \mathbf{v}^h = \sum_i \begin{bmatrix} \mathrm{v}_{2i} \\ \mathrm{v}_{2i+1} \end{bmatrix} \varphi_i = \sum_j \mathrm{v}_j \boldsymbol{\varphi}_j \tag{6}$$

$$p^h = \sum_j \mathrm{p}_j \psi_j \tag{7}$$

(and similarly for $\mathbf{w}^h$ and q^h) where the superscript h denotes the discretized version. To relax the incompressibility condition in order to avoid mesh locking, the support of functions ψ_i is chosen to be triangles adjacent to vertex i, where ψ_i is 1, and zero elsewhere. Consequently, we have $2N_u$ degrees of freedom for each $\mathbf{v}_t$, N_v degrees of freedom for μ and each p_t and q_t, and N_i degrees of freedom for each $\mathbf{w}_t$. Note also that with this discretization, the bilinear form A (4) can be integrated exactly.

The discretized state $\boldsymbol{\xi}^h$ of the modulus and displacement reconstruction problem is completely described by a finite-dimensional state vector $\boldsymbol{\Xi}$ with $N_x = n(2N_u + N_v) + N_v$ degrees of freedom.

$$\boldsymbol{\xi}^h \stackrel{\text{def}}{=} \big(\mu^h, \{\mathbf{v}_t^h\}, \{p_t^h\}\big) \longleftrightarrow \boldsymbol{\Xi} = \big(\{\mathrm{m}_i\}, \{\mathrm{v}_{j,t}\}, \{\mathrm{p}_{k,t}\}\big) \in \mathbb{R}^{N_x} \qquad t \neq 0$$

The corresponding discretized version of the manifold (5) of consistent solutions is

$$\mathcal{C}^h = \Big\{\boldsymbol{\xi}^h = \big(\mu^h, \{\mathbf{v}_t^h\}, \{p_t^h\}\big); \mu^h > 0, \mathbf{c}(\boldsymbol{\xi}^h) = \mathbf{0}\Big\}$$

with a vector of constraints

$$\mathbf{c}(\boldsymbol{\xi}^h) = D_{\boldsymbol{\lambda}} A^h(\boldsymbol{\xi}^h, \mathbf{w}^h, q^H) \quad \text{and} \quad \begin{bmatrix}\mathbf{w}^h \\ q^h\end{bmatrix} = \boldsymbol{\Phi}\boldsymbol{\lambda}$$

where $\boldsymbol{\lambda} = \big(\{\mathrm{w}_{i,t}\}, \{\mathrm{q}_{j,t}\}\big)$ is a vector expressing the test functions $\mathbf{w}^h$ and q^h using P1 and P0 basis functions (6),(7). As A^h is linear in $\boldsymbol{\lambda}$, we have $\forall \boldsymbol{\lambda}; A^h(\boldsymbol{\xi}^h, \boldsymbol{\lambda}) = 0$ iff $\mathbf{c}(\boldsymbol{\xi}^h) = D_{\boldsymbol{\lambda}} A^h(\boldsymbol{\xi}^h, \boldsymbol{\lambda}) = \mathbf{0}$. To simplify the notation, we will from now on drop the superscript h even if the resulting algorithm must obviously represent the continuous quantities in the appropriate finite dimensional bases.

2.5 Image similarity criterion

A solution $\boldsymbol{\xi} = \big(\mu, \{\mathbf{v}_t\}, \{p_t\}\big)$, besides satisfying the elasticity constraints, must also be consistent with the image sequence $\{f_t\}$. The displacements $\mathbf{v}_t^h$ must correspond to the observed movement in the image sequence. The similarity between a pair of images f, g is measured by a normalized version of the SSD criterion

$$J_s(f,g) = \frac{1}{2} \frac{\displaystyle\sum_{\mathbf{i}\in I} m_g(\mathbf{i})\, m_f(\mathbf{i}) \, \Big(g(\mathbf{i}) - f(\mathbf{i})\Big)^2}{\displaystyle\sum_{\mathbf{i}\in I} m_g(\mathbf{i})\, g(\mathbf{i})^2 + m_f(\mathbf{i}) f(\mathbf{i})^2}$$

where I is the set of pixel coordinates in the images and m_f and m_g are masks, determining the region of interest. There is one mask m_t associated with each image f_t. This criterion is fast to calculate, invariant to image intensity scale changes and largely insensitive to changes of overlap. This is important in our application where the imaged region is changing from frame to frame. We chose to evaluate the similarity between the reference image f_0 and deformed images $\big(T_{\mathbf{u}_t} f_t\big)(\mathbf{x}) = f_t\big(\mathbf{u}_t(\mathbf{x})\big)$, where $\mathbf{u}_t$ and $\mathbf{v}_t$ are recursively related by (1)

$$\mathbf{u}_t(\mathbf{x}) = \mathbf{u}_{t-}(\mathbf{x}) + \mathbf{v}_t\big(\mathbf{u}_{t-}(\mathbf{x})\big) \quad \text{and} \quad \mathbf{u}_0(\mathbf{x}) = \mathbf{x}$$

In our experience [19, 20] comparing each image with a reference is more accurate than evaluating the similarity between adjacent images. Bilinear interpolation

and zero boundary conditions are used to evaluate the warped image $T_{\mathbf{u}_t} f_t$ and the corresponding warped mask $T_{\mathbf{u}_t} m_t$. The global similarity criterion over the whole sequence is:

$$J(\boldsymbol{\xi}) = J\big(\{\mathbf{v}_t\}\big) = \sum_{t \neq 0} J_s(f_0, T_{\mathbf{u}_t} f_t)$$

2.6 Problem definition

Given the definitions above our problem of simultaneous reconstruction of elastic properties of the tissue and the displacements consistent with the elasticity equations and the acquired image sequence can be described as a constrained optimization:

$$\boldsymbol{\xi}^* = \arg\min_{\boldsymbol{\xi}} J(\boldsymbol{\xi}) \quad \text{for} \quad \boldsymbol{\xi} \in \mathcal{C} \tag{8}$$

The difficulty lies in the complicated nonlinear structure of the manifold $\mathcal{C}$, coming from the $\mu \nabla^s \mathbf{v}_t$ products (4) and the the displacement accumulation $\{\mathbf{v}_t\} \mapsto \{\mathbf{u}_t\}$. In other words, the PDE (2) is solved in a curved space, the local curvature of which is influenced by the deformation in preceding frames. The problem (8) may have several local minima. Therefore, finding a good starting point $\boldsymbol{\xi}_0$ is important. Usually, we use $\mathbf{v}_t = \mathbf{0}$, $p_t = 0$, and $\mu = 1$, or multiresolution (Section 2.8).

According to our tests, most higher-order approximations used by standard optimization methods are only useful in a close vicinity of the solution point. We therefore chose a modified trust region optimization method [21], described in the following section, as it was the only method tested providing the required robustness.

2.7 Trust region optimization

In contrast to the classical trust region approach that uses linearized constraints and quadratic approximation to the criterion, we found that a linear approximation of the criterion is adequate, while the constraints have to be take into account exactly in each step, otherwise the convergence is not ensured.

Major iterations. Starting from an initial (feasible) estimate $\boldsymbol{\xi}_0$, the trust region optimizer attempts to find a sequence of estimates $\boldsymbol{\xi}_0, \boldsymbol{\xi}_1, \boldsymbol{\xi}_2, \ldots$ on the manifold $\mathcal{C}$, (i.e., such that $\mathbf{c}(\boldsymbol{\xi}_i) = \mathbf{0}$ for all i), and so that further the sequence of criterion values $J(\boldsymbol{\xi}_0), J(\boldsymbol{\xi}_1), J(\boldsymbol{\xi}_2), \ldots$ is decreasing. Each step $\boldsymbol{\xi}_i \rightarrow \boldsymbol{\xi}_{i+1}$ is termed a major iteration. Major iterations terminate if the decrease of J is below an a priori chosen relative or absolute threshold (we normally use a relative threshold of 10^{-3}) or if the process stagnates (no improvement can be found).

Within each major iteration i, we linearize the criterion around $\boldsymbol{\xi}_i$

$$\tilde{J}(\boldsymbol{\xi}_i + \mathbf{z}) = J(\boldsymbol{\xi}) + D_{\boldsymbol{\xi}} J(\boldsymbol{\xi}_i)\, \mathbf{z} = J_i + \mathbf{a}^T \mathbf{z} \tag{9}$$

and solve the reduced problem

$$\mathbf{z}^* = \arg\min \tilde{J}(\boldsymbol{\xi}_i + \mathbf{z}) = \arg\min \mathbf{a}^T\mathbf{z} \qquad \text{for} \qquad \mathbf{z} + \boldsymbol{\xi}_i \in \mathcal{C}, \quad \|\mathbf{z}\| < \varrho_i \quad (10)$$

where ϱ_i is the trust region radius. We start with $\varrho_0 = 0.3$ (units of ϱ partly correspond to pixels). If the problem (10) is successfully solved and $J(\boldsymbol{\xi}_i + \mathbf{z}^*) < J(\boldsymbol{\xi}_i)$ (the linear approximation is valid), we accept the step by setting $\boldsymbol{\xi}_{i+1} = \boldsymbol{\xi}_i + \mathbf{z}^*$ and increase $\varrho_{i+1} = 1.5\varrho_i$. Otherwise, we try to solve (10) again with $\varrho_i \leftarrow 0.1\varrho_i$.

The problem (10) is equivalent to

$$\mathbf{z}^* = \arg\min \mathbf{a}^T\mathbf{z} + \frac{\alpha}{2}\|\mathbf{z}\|^2 \quad \text{for} \quad \mathbf{z} + \boldsymbol{\xi}_i \in \mathcal{C} \qquad (11)$$

for some Lagrange multiplier α. The appropriate α is found by a binary search, stopping if $0.1\varrho \le \|\mathbf{z}\| \le \varrho$ and using the last value of α as a first guess. If no such α can be found, the major iteration is declared to fail.

Minor iterations. The problem (11) is again solved iteratively, producing a sequence $\mathbf{z}_0, \mathbf{z}_1, \ldots$. Each step is called a minor iteration. The first of them, $\mathbf{z}_0$ is chosen to minimize (9) in the trust region, regardless of the constraints

$$\mathbf{z}_0 = \arg\min \mathbf{a}^T\mathbf{z} \quad \text{for} \quad \|\mathbf{z}\| \le \varrho \qquad (12)$$

The solution (except degenerate cases) is $\mathbf{z}_0 = -\varrho\mathbf{a}/\|\mathbf{a}\|$. Then, for each minor iteration estimate $\mathbf{z}_j$ we find the next estimate $\mathbf{z}_{j+1}$ as a solution to the constrained optimization problem (11) with linearized constraints

$$\begin{aligned} \mathbf{z}_{j+1} &= \arg\min_{\mathbf{z}} \mathbf{a}^T\mathbf{z} + \frac{\alpha}{2}\|\mathbf{z}\|^2 \\ \text{with} \quad \mathbf{0} &= \mathbf{d} + \mathsf{B}(\mathbf{z} - \mathbf{z}_j) \\ \text{where} \quad \mathbf{d} + \mathsf{B}(\mathbf{z} - \mathbf{z}_j) &= \mathbf{c}(\boldsymbol{\xi}_i + \mathbf{z}_j) + \big(D_{\boldsymbol{\xi}}\, \mathbf{c}(\boldsymbol{\xi}_i + \mathbf{z}_j)\big)\,(\mathbf{z} - \mathbf{z}_j) \approx \mathbf{c}(\boldsymbol{\xi}_i + \mathbf{z}) \end{aligned}$$

We form the Lagrangian

$$\mathscr{L} = \mathbf{a}^T\mathbf{z} + \frac{\alpha}{2}\|\mathbf{z}\|^2 + \mathbf{y}^T\big(\mathbf{d} + \mathsf{B}(\mathbf{z} - \mathbf{z}_j)\big)$$

and find its first order optimality conditions for $\delta\mathbf{z} = \mathbf{z}_{j+1} - \mathbf{z}_j$:

$$\begin{aligned} \alpha\,\delta\mathbf{z} \quad + \mathsf{B}^T\mathbf{y} &= -\mathbf{a} - \alpha\mathbf{z}_j \\ \mathsf{B}\,\delta\mathbf{z} \qquad\quad &= -\mathbf{d} \end{aligned} \qquad (13)$$

The sparse symmetric linear system of equations (13) is solved using the (iterative) MINRES method [22].

We monitor the constraint fulfillment $\|\mathbf{c}(\boldsymbol{\xi}_i + \mathbf{z}_j)\|$ during minor iterations. Normally only a few iterations ($3 \sim 5$) are needed to ensure that the dicrepancy is sufficiently small ($\|\mathbf{c}(\boldsymbol{\xi}_i + \mathbf{z}_j)\| < 10^{-4}$). If divergence is detected (the discrepancy $\|\mathbf{c}(\cdot)\|$ increases), the minor iterations are declared to fail. Consequently, in the next major iteration, smaller ϱ will be used and so the linear approximation of the constraints will be more accurate and the major iterations thus less likely to diverge.

Summary of the trust region optimization. The trust region algorithm consists of four cascaded iteration loops. The outermost, major iterations, finds a sequence of feasible solutions $\boldsymbol{\xi}_i$ with decreasing criterion values. The second level attempts to find a suitable value α such that the step $\mathbf{z}^*$ of (11) has a correct amplitude $\|\mathbf{z}^*\| \leq \varrho$. The third level (minor iterations) iteratively solves (11). Finally, the innermost, fourth level, iteratively solves a linear system of equation (13) within each minor iteration.

Unfeasible starting points. If only an infeasible (not belonging to $\mathcal{C}$) starting point $\boldsymbol{\xi}'_0$ is available, we project it to $\mathcal{C}$ by minimizing

$$\boldsymbol{\xi}_0 = \arg\min_{\boldsymbol{\xi}} \|\boldsymbol{\xi} - \boldsymbol{\xi}'_0\|^2_W \quad \text{for} \quad \boldsymbol{\xi} \in \mathcal{C} \tag{14}$$

where $\|(\mu, \{\mathbf{v}_t\}, \{p_t\})\|^2_W = 10^3\|\mu\|^2 + \|\{\mathbf{v}_t\}\|^2 + \|\{p_t\}\|^2$ is a weighted Euclidean norm which gives more weight to the μ components of $\boldsymbol{\xi}$, expressing our a priori estimate of the precision of the various components. The minimization problem (14) is solved by repeated projections to the linearized constraint subspace with respect to $\|\cdot\|_W$, until convergence is reached, similarly to the minor iterations described above (13). Infeasible starting point may arise for example when interpolating a coarse solution in a multiresolution framework (Section 2.8). Normally, however, the distance from the constraint space is small, just due to numerical errors, so only a few iterations are needed and the choice of the projection norm is not crucial.

Maintaining feasibility. We had to add two additional rules to the evaluation of the success of each major iteration, preventing the algorithm from running astray. First, we require that μ is everywhere positive. If not, we project the proposed μ to the allowed space by selectively setting the offending components to small positive numbers (10^{-6}). Second, we require that the change of all accumulated displacements $\mathbf{u}_t$ be less than 0.5 pixels in magnitude everywhere. Both rules could be implemented within the trust region approach albeit with a slightly higher computational cost. We opted for this hybrid approach since both rules only affect the optimization during a few initial steps.

2.8 Multiresolution

To improve speed and robustness of the optimizer, a multiresolution approach was used with respect to both mesh and image size. We start with a coarse mesh and coarse versions of the images — normally a mesh with 3×3 nodes and images of about 64×64 pixels are used. Once the coarse problem is solved (which is fast), its solution is used as a starting point for a finer one. In the outer loop we progressively refine the mesh by subdivision. In the inner loop, we increase the image resolution, so that the problem is solved at optimum level — as a rule of thumb, we attempt to have image size $5l \sim 10l$ pixels, where l is the maximum edge length for the mesh. We continue until the desired mesh

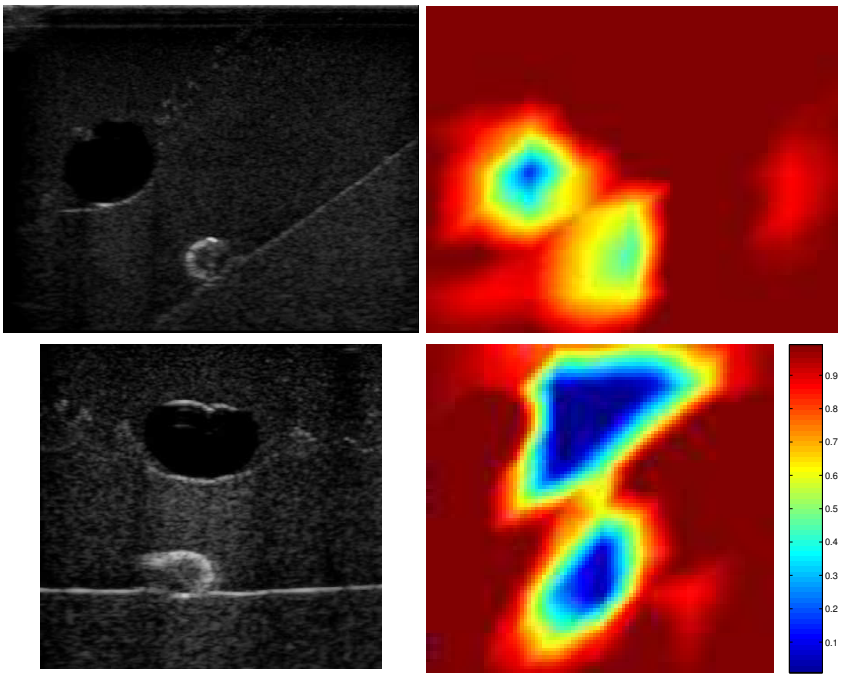

Fig. 2. Phantom images (left column) and corresponding reconstruction of the relative modulus μ from sets of 3 images with a 10×10 node mesh (right column). The same color scale is used in both images.

and image resolution is reached. The image pyramid is built by convolution with a 3×3 smoothing filter and down-sampling by a factor of 2.

When the mesh or image resolution is changed, the status vector $\boldsymbol{\xi}$ must be updated accordingly. This involves multiplying $\mathbf{v}_t$ by 2 (for image size change) or taking the mean of the parent node values (for mesh expansion). The interpolated state vector has to be projected to $\mathcal{C}$ (see (14)).

3 Experiments

First experiment is based on data acquired on a Gammex 429 Ultrasound Biopsy Phantom[3] that mimics normal breast tissue and contains eleven test objects filled with low or high density gel, simulating lesions (Figure 2). Two of the acquired images with different views of different lesions are shown, each representing a whole sequence. Corresponding reconstructions using 3 images are shown; using 2 images did not converge to an acceptable solution, using more than 3 images did not improve the results significantly.

[3] `www.gamex.com`

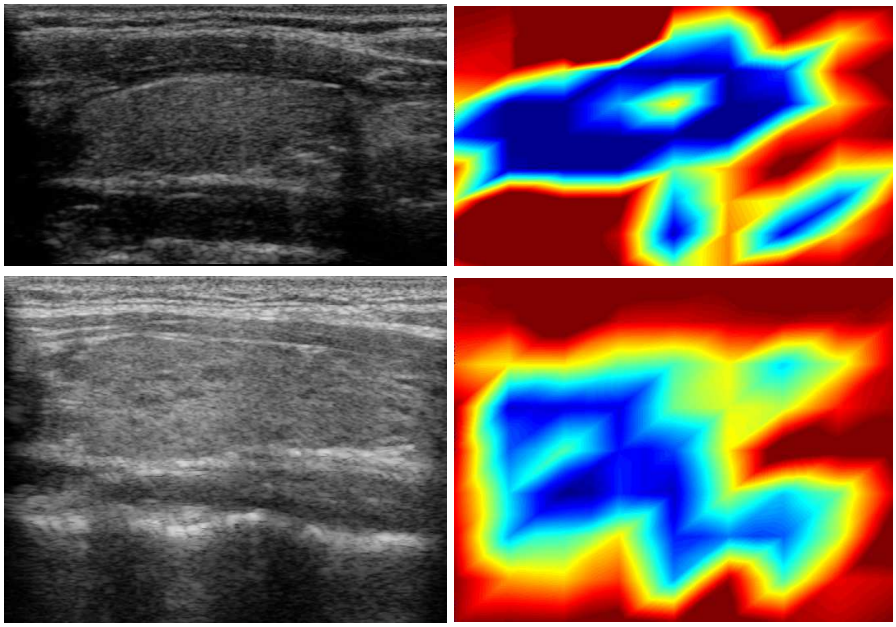

Fig. 3. Normal thyroid gland image (top left) and the reconstructed elastogram from a 3 image set (top right). Acute thyroiditis subject image (bottom left) and the corresponding elastogram reconstructed using a finer mesh and 5 images (bottom right). The same color scale is used as in Fig. 2.

Figure 3 (top) shows a reconstruction based on a real thyroid gland ultrasound sequence of a normal subject using 3 images. Finally, for illustration, the bottom image shows a reconstruction from thyroid gland sequence taken from a subject with acute thyroiditis, [4] reconstructed using a twice finer mesh and 5 images.

4 Timings and resolution

Most reconstructions shown above used 3 images of about 500×500 pixels and moderate density meshes with about 10×10 nodes. Such reconstruction takes 10 min $\sim$ 1 h on a standard PC (1.4 GHz Pentium). The time increases significantly with both mesh density and number of images. As an illustration, the thyroiditis reconstruction above with 20×20 nodes and 5 images took over 5 h.

[4] We suspect there might be a difference in the elastic properties however it probably is not discernible at the current resolution level of the elastograms.

5 Conclusions

We have presented an algorithm for simultaneous estimation of displacement field and shear modulus distribution from a series of standard ultrasound images. The novelty of the method is in its ability of combining information from several images in a global manner. It is based on the theoretical observation that while reconstructing a shear modulus from a pair of images is bound to lead to an ill-defined problem [17], the situation is improved if several deformation fields are available. This way we avoid inventing essentially unmeasurable boundary data for the direct elasticity problem. The reconstruction task is formulated as a constrained optimization method. Unfortunately, since we no longer have a uniquely solvable direct problem, the feasible subspace that needs to be searched is a highly convoluted manifold of all solutions consistent with linear elasticity equations. Therefore, the computation time is rather long. Also, since our data is relatively noisy and low resolution, we suspect there might not even be enough information to obtain more details of the shear modulus distribution. In any case, the new method gives better results than the previous algorithm [14], based on only two images.

Acknowledgements

The first author was sponsored by the Czech Ministry of Education, grant MSM6840770012, the second author by the Grant Agency of the Czech Academy of Sciences, grant 1ET101050403.

References

1. J. Ophir, F. Kallel, T. Varghese, E.E. Konofagou, S. K. Alam, B. Garra, T. Krouskop, and R. Righetti, "Elastography: Optical and acoustic imaging of acoustic media," *C. R. Acad. Sci. Paris*, vol. 2, no. 8, pp. 1193–1212, 2001, serie IV.
2. M. F. Insana, L. T. Cook, and Chaturvedi P., "Analytical study of bioelasticity ultrasound systems.," in *Information Processing in Medical Imaging (IPMI)*, Kuba A., Samal M., and Todd-Pokropek A., Eds. Berlin, 1999.
3. H. T. Liu and L. Z. Sun, "Analytic modeling of breast elastography," *Medical Physics*, vol. 30, no. 9, pp. 2340–2349, Sept. 2003.
4. Wen-Chun Yeh, Pai-Chi Li, Yung-Ming Jeng, Hey-Chi Hsu, Po-Ling Kuo, Meng-Lin Li, Pei-Ming Yang, and Po Huang Lee, "Elastic modulus measurements of human liver and correlation with pathology," *Ultrasound in Medicine & Biology*, vol. 28, no. 4, pp. 467–474, apr 2002.
5. Yin, Sun, Wang, and M. Vannier, "Modeling of elastic modulus evolution of cirrhotic human liver," *IEEE Trans. Biomed Eng.*, vol. 51, no. 10, pp. 1854–1856, Oct. 2004.
6. Ji Lin and J. McLaughlin, "Recovery of the Lamé parameter μ in biological tissues," *Inverse Problems*, , no. 20, pp. 1–24, 2004.
7. J. R. McLaughlin and Yoon J.-R., "Unique identifiability of elastic parameters from time-dependent interior displacement measurement," *Inverse Problems*, , no. 20, pp. 24–45, 2004.

8. J. Bishop, A. Samani, J. Sciaretta, and Plewes D. B., "Two-dimensional MR elastography with linear inversion reconstruction: methodology and noise analysis," *Phys. Med. Biol.*, , no. 45, pp. 2081–2091, 2000.
9. H. Liu and P. Shi, "Robust identification of object elasticity," in *Computer Vision and Mathematical Methods in Medical and Biomedical Image Analysis (CVAMIA+MMBIA)*, Milan Šonka, A. Ioannis Kakadiaris, and Jan Kybic, Eds., number 3117 in Lecture Notes in Computer Science, pp. 423–435. Springer, Heidelberg, May 2004.
10. A. Oberai, N. Gokhale, and G. Feijóo, "Solution of inverse problems in elasticity imaging using the adjoint method," *Inverse Problems*, , no. 19, pp. 297–313, 2003.
11. S. Srinivasan and J. Ophir, "A zero-crossing strain estimator for elastography," *Ultrasound in Medicine and Biology*, vol. 29, no. 2, pp. 227–238, Feb. 2003.
12. E. Brusseau, J. Fromageau, N. Rognin, P. Delacharte, and D. Vray, "Local estimation of RF ultrasound signal compression for axial strain imaging: theoretical developments and experimental design," *IEEE Engineering in Medicine and Biology Magazine*, vol. 21, no. 4, pp. 86–94, July 2002.
13. Paul Barbone, Nachiket Gokhale, Michael Richards, Assad Oberai, and Marvin Doyley, "Simultaneous elastic image registration and elastic modulus reconstruction.," in *Proceedings of the 2004 IEEE International Symposium on Biomedical Imaging: From Nano to Macro, Arlington, VA, USA, 15-18 April 2004*. 2004, pp. 543–546, IEEE.
14. Jan Kybic and Daniel Smutek, "Estimating elastic properties of tissues from standard 2d ultrasound images," in *Proceedings of the SPIE Conference on Medical Imaging*. July 2005, SPIE.
15. C. W. Washington and M. I. Miga, "Modality independent elastography (MIE): A new approach to elasticity imaging," *IEEE Transactions on Medical Imaging*, pp. 1117–1126, Sept. 2004.
16. P. E. Barbone and J. C. Bamber, "Quantitative elasticity imaging: what can and cannot be inferred from strain images," *Phys. Med. Biol.*, , no. 47, pp. 2147–2164, 2002.
17. P. E. Barbone and N. H. Gokhale, "Elastic modulus imaging: on the uniqueness and nonuniqueness of the elastography inverse problem in two dimensions," *Inverse Problems*, , no. 20, pp. 283–296, 2004.
18. J. Nečas and I. Hlaváček, *Mathematical Theory of Elastic and Elasto-Plastic Bodies*, Elsevier, Amsterdam, 1981.
19. María J. Ledesmay-Carbayo, Jan Kybic, Manuel Desco, Andrés Santos, and Michael Unser, "Cardiac motion analysis from ultrasound sequences using non-rigid registration," in *Proceedings of MICCAI*, Wiro J. Niessen and Max A. Viergever, Eds. October 2001, pp. 889–896, Springer-Verlag.
20. Maria Jesus Ledesma-Carbayo, Jan Kybic, Michael Sühling, P. Hunziger, M. Desco, A. Santos, and M. Unser, "Cardiac ultrasound motion detection by elastic registration exploiting temporal coherence," in *Proceedings of the First 2002 IEEE International Symposium on Biomedical Imaging: Macro to Nano (ISBI'02)*, 445 Hoes Lane, Piscataway, NJ, U.S.A., July 2002, pp. 585 – 588, IEEE.
21. J.J. Moré and D.C. Sorensen, "Computing a trust region step," *SIAM Journal on Scientific and Statistical Computing*, pp. 553–572, 1983.
22. Richard Barret, Michael Berry, Tony F. Chan, James Demmel, June Donato, Jack Dongarra, Victor Eijkhout, Roldan Pozo, Charles Romine, and Henk van der Vonst, *Templates for the Solution of Linear Systems: Building Blocks for Iterative Methods*, SIAM, Philadelphia, 1994, Available from netlib.